Finite kinematics diffuse interface mechanics coupled to solid composite propellant deflagration

Maycon Meier[a], Brandon Runnels[b,a,*]

[a]Department of Mechanical and Aerospace Engineering, University of Colorado, Colorado Springs, CO, USA
[b]Department of Aerospace Engineering, Iowa State University, Ames, IA, USA

ARTICLE INFO

Keywords:
Solid rocket motors
Combustion
Diffuse interface methods
Computational mechanics
Computational physics

ABSTRACT

Solid Composite Propellants (SCPs) are widely employed in the field of propulsion due to their enduring chemical and mechanical stability during extended periods of storage, as well as their uncomplicated production and reliable performance. Unlike liquid propellants, solid propellants are self-supporting, meaning that that they function as structural materials as well as energetic. Consequently, it is essential to understand the mechanical behavior of SCPs during deflagration, as structural failure can have potentially catastrophic consequences. SCP failure is often associated with the formation and growth of micromechanical damage sites due to thermal and mechanical loads during burning. Thus, the ability to simulate stress propagation during the burning process is a key feature for the effective design and safe use of SCPs. The ability to evaluate failure in aged propellants and of those produced using additive manufacturing is of special interest. In this work, we present an elasticity solver coupled with a thermal phase-field model of regression of SCPs. The method implements a unique strong-form solver for finite deformation material response, featuring block structured adaptive mesh refinement techniques and a multigrid solver. Two verification results for the model are presented: first, results for an infinite plate with a pressurized hole is compared to the classical Lamé solution; second, results for a clamped plate with a hole subjected to uniaxial tension are compared to the equivalent results using the traditional finite element. In both cases, a close match is observed. Next, to test the model for the application of SCPs, tension-compression tests are used to validate the model for AP/HTPB under tension. The model is then used to determine the mechanical response of an AP/HTPB SCP during deflagration, driven both by thermal and mechanical loading, with both spherical and experimentally measured mesostructures. Overall, it is determined that the model adequately captures the stress and strain fields, indicating the model's viability for simulations that lend insight into the interplay between mesostructure, deflagration, and mechanical damage.

1. Introduction

Solid Composite Propellants (SCPs) have played a pivotal role in rocket and missile propulsion for over a century. Though slightly less efficient than liquid propellants, SCPs offer many advantages due to their simple production and storage, self-support and self-actuation, and overall mechanical/chemical stability. A key advantage of these propellants is that their burning behavior can not be changed after ignition has started, which leads to the need for careful design [1]. The thrust generated by SCPs is directly correlated with the total area of the burning interface so the existence and propagation of cracks can be a major source of failure.

SCPs are energetic composites that are commonly composed of an oxidizer, such as ammonium perchlorate (AP), a fuel binder, such as hydroxyl-terminated polybutadiene (HTPB), and additives such as aluminum [2–4]. SCPs are often stored in environments without temperature control. While they are generally stable, they can nevertheless suffer from thermal strains over time that can cause void nucleation due to dewetting processes[5]. The constituent materials also undergo slow decomposition as they age, which can lead to degradation of the original geometry [5]. Moreover, as additive manufacturing (AM) of SCPs becomes more and more feasible, it is essential to determine the effect of AM processes on mesostructure and, eventually, failure likelihood. Experimental characterization of these mechanisms is expensive and often hazardous, and to the best of the authors' knowledge, there is no way to determine mechanical response *in situ* during deflagration. Computational simulations are a necessary recourse to assess the behavior of these

*Corresponding author
brunnels@iastate.edu (B. Runnels)
ORCID(s): 0000-0001-9914-8811 (M. Meier); 0000-0003-3043-5227 (B. Runnels)

materials, but it is very complex since these materials are heterogeneous at a microscale with significantly different properties, burning behavior, and stress responses.

Despite the need for predictive analysis of SCP mechanics during deflagration, numerical modeling efforts have been relatively limited. To solve the basic regression problem (sans mechanics) a number of methods have been proposed: these include level set methods [6, 7], coordinate-mapping [6, 8–10], and the phase field method [11, 12] proposed recently by the authors. On the other hand, fundamental mechanics studies have focused on basic damage mechanisms such as fracture during the burn regression [13–15], isothermal damage [16], and thermally varying damage models with linear elasticity [17–19], along with the associated computational implementation [5, 20–22]. Prior studies of the thermomechanical response of SCPs during deflagration have been primarily in the context of discrete solid-solid and solid-gas interfaces. Specifically, Srinivasan, Matouš, Geubelle, and Jackson [23] coupled the generalized finite element method (GFEM) to the level-set method to investigate the mechanical response of an SCP consisting of spherical particles. On the other hand, a 3D investigation of thermal-elastic response couple to an Eulerian coordinate mapping model was recently presented in Kumar and Jackson [24]; extending the method proposed by Kumar, Rycroft, and Jackson [9]. The thermomechanical response of an SCP described with fully implicit diffuse interfaces, however, remains unexplored.

The problem of mechanical analysis of propellants during burn is challenging for many reasons, which we summarize here. (1) The timescale of deflagration is much longer than the acoustic timescale, meaning that the mechanical response is quasistatic and must be solved implicitly, whereas regression models are usually designed in the context of a fully-explicit Eulerian solver. (2) The deflagration process inherently involves drastic changes in geometry, which is notoriously difficult to capture in usual mechanics methods such as finite element. (3) The mesostructure of realistic propellants usually differs considerably from idealized, packed-spheres-type structures often required for most regression models. These challenges indicate that an alternative approach is needed.

In this work, we present a diffuse interface method for large mechanical deformation. The model is verified against both theoretical and finite element results, and then used to predict mechanical response of SCPs during deflagration, as driven by the associated thermal and mechanical loads. This work combines the previously reported phase field regression model [12] with a strong-form diffuse interface mechanics solver that was originally presented for linear elastic solids by Agrawal and Runnels [25]. It advances the previous development by combining the diffuse interface near-singular mechanics formulation with finite kinematics. There are numerous advantages to this approach. Because both methods rely on the diffuse interface approximation, they may be coupled together in a direct and natural way. This makes it efficient and convenient to effect bidirectional coupling between the deflagration and the mechanical response. Moreover, the use of adaptive mesh refinement with a diffuse species field makes it possible to simulate realistic propellants, rather than idealized structures.

The remainder of the paper is structured in the following way. Section 2 provides an overview of the phase field regression and thermal transport models, followed by a thorough presentation of the strong-form mechanics finite kinematics solver. In Section 3, a brief discussion of the computational methods is presented. Section 4 presents a selection of results to verify and demonstrate the use of the model: (i) verification against theoretical and finite element solutions, (ii) tension and thermal expansion tests in 2D and 3D, (iii) thermomechanical response of a packed spheres SCP during deflagration, and (iv) thermomechanical response of a realistic microstructure during deflagration. Finally, Section 5 summarizes the findings and provides recommendations for the use and future development of the model.

2. Modeling

This section provides a complete overview of the modeling methodology. The first two sections outline, for completeness, a terse yet comprehensive overview of the previously developed regression and thermal evolution models. The third section introduces the strong-form, finite difference mechanics solver for near-singular problems.

2.1. Phase-field modeling

This section reviews the full-feedback phase field regression model. References [11, 12] are general references for this section, and may be consulted for additional detail and application examples. Begin by defining continuum region $\Omega \subset \mathbb{R}^n$, $n = 2, 3$ that contains the unburned SCP. Two tracking fields $\eta \in H(\Omega[0, 1])$ and $\phi \in H(\Omega[0, 1])$, called order parameters, map from Ω to the unit interval. The field η defines the burned state of the SCP: $\eta = 1$ corresponds to unburned (solid), and $\eta = 0$ to burned (gas). The field ϕ discriminates between different materials in the system,

and is assumed differentiable. For this work, $\phi = 1$ indicates AP, $\phi = 0$ indicates HTPB. Other materials (such as metal additives) or phases (such as a melt layer) are not considered here.

The physics of the problem are encapsulated in the free energy function $f : H\ \Omega[0, 1] \to \mathbb{R}$, which is constructed with the form:

$$f[\eta] = \int_{\Omega} \left[\lambda w(\eta) + \frac{1}{2}\epsilon^2 \kappa |\nabla \eta|^2 \right] \mathrm{d}x, \tag{1}$$

where ω is a chemical potential (typically a fourth-order polynomial), λ is a non-dimensionalized scaling factor representing a Lagrange multiplier, and κ is the interface energy. ϵ is the interface length scale parameter, controlling the diffusiveness of the solid/gas boundary. As $\epsilon \to 0$, the diffuse interface solution approaches the sharp interface solution. It is worth emphasizing that the main benefit of this formulation is the implicit tracking of the interface that is provided by the use of the order parameter η and does not require any additional computation steps. Moreover, the material properties are also easily captured by ϕ, leading to an overall simple and efficient solution. The evolution of the unburned region, therefore, is determined by the partial differential equation,

$$\frac{\mathrm{d}\eta}{\mathrm{d}t} = -\frac{L}{\epsilon}\frac{\delta f}{\delta \eta} = -L(\boldsymbol{x}) \left[\frac{\lambda}{\epsilon} \frac{\mathrm{d}w(\eta(\boldsymbol{x}))}{\mathrm{d}\eta} - \epsilon \kappa \Delta \eta(\boldsymbol{x}) \right], \tag{2}$$

where L is a rate constant that controls the rate of regression in the system. The rate constant is determined by the Arrhenius law

$$L = A(\phi(\boldsymbol{x})) \exp\left(\frac{-E_{\mathrm{a}}(\phi(\boldsymbol{x}))}{R_{\mathrm{u}} T(\boldsymbol{x})} \right), \tag{3}$$

where R is the universal gas constant and T is the temperature. A and E are, respectively, the pre-exponential factor and the activation energy, which are material-specific properties that are obtained from the literature.

2.2. Heat equation

Equation (3) requires information about local temperature, which necessitates the solution of the heat equation, driven by gas-phase heat flux, in the diffuse boundary framework. Given a heat flux $\boldsymbol{q}$ imparted to the diffuse burn surface by the gas phase, the thermal evolution within the SCP is,

$$k\nabla(\eta T) - \eta \boldsymbol{q} = \nabla \eta\, k\, T_0 \qquad\qquad \eta \rho c_p \frac{\partial T}{\partial t} - \eta \nabla \cdot \boldsymbol{q} = 0, \tag{4}$$

where k is the thermal conductivity, ρ is the density, and c_p is the specific heat. All material properties are assumed to vary spatially. (It may be shown, following Theorem 1 in [26], that Eq. (4) converges exactly to the discrete boundary formulation in the sharp interface limit.) For purposes of implementation, Eq. (4) are combined as

$$\eta \frac{\partial T}{\partial t} = \frac{1}{\rho c} \nabla \cdot (\eta\, k\, \nabla T) + |\nabla \eta| \frac{q_0}{\rho c}. \tag{5}$$

It is known that solving Eq. (5) for the solid phase can produce instabilities as $\eta \to 0$, causing the temperature values to grow too fast. To resolve this issue, a "stand-in" is used, allowing for smooth convergence of the temperature without decreasing the time step without affecting the solution. The stand-in is implemented as follows:

$$T_{\mathrm{total}} = \eta T_{\mathrm{solid}} + (1 - \eta) T_{\mathrm{fluid}}, \tag{6}$$

where T_{fluid} is the fluid stand-in and it is set to a constant value. The ηT_{solid} term is then evolved separately by

$$\left. \frac{\mathrm{d}\left(\eta T_{\mathrm{solid}}\right)}{\mathrm{d}t} \right|_t = \eta|_{t-1} \left. \frac{\partial T_{\mathrm{solid}}}{\partial t} \right|_t + T_{\mathrm{solid}}|_{t-1} \left. \frac{\partial \eta}{\partial t} \right|_t. \tag{7}$$

Following [12], we use the data from Gross and Beckstead [27] to estimate the flux from the gas phase, noting that a full gas-phase solver may substantially improve the heat flux estimate and will constitute future work.

2.3. Strong form elasticity

In this section, we present the diffuse boundary formulation of the mechanics of a deformable body with finite deformation kinematics. Assuming that the body occupies the unburned region, $\Omega \subset \mathbb{R}^3$, behavior is dictated by the principle of stationary action, i.e.

$$\delta(\mathrm{T} - \Pi) = 0 \tag{8}$$

where T and Π are the kinetic and potential energies, respectively, and δ is the variation of the energy difference (that is, the action) with respect to all kinematic degrees of freedom. SCPs are typically made of materials with significant compliance, prompting the need for nonlinear kinematics. We establish the deformation mapping $\boldsymbol{x} : \mathbb{R} \times \Omega \to \mathbb{R}^3$ (note that non-vector $\boldsymbol{\phi}$ is used elsewhere to denote diffuse species field) and the conventional notation:

$$\boldsymbol{x} = \boldsymbol{x}(\boldsymbol{X}, t) \tag{9}$$

where uppercase and lowercase letters indicate the Lagrangian and Eulerian frames, respectively. The time scale of deflagration is significantly longer than that of the material sound speed, so the quasistatic approximation $T \approx 0$ is appropriate. This enables the transition from the principle of stationary action to the principle of minimum potential energy, i.e.

$$\boldsymbol{\phi}^* = \arg\inf_{\boldsymbol{\phi}} \ \Pi[\boldsymbol{\phi}], \tag{10}$$

where the asterisk indicates the equilibrium value, and square brackets are understood to indicate dependency on spatial and temporal derivatives of the argument. The usual form is adopted for potential energy:

$$\Pi[\boldsymbol{\phi}] = \int_\Omega \Big[\mathrm{W}(\mathbf{F}) - \boldsymbol{x} \cdot \mathbf{B} \Big] \, d\lambda(\boldsymbol{X}) - \int_{\partial_2 \Omega} \boldsymbol{x} \cdot \mathbf{T} \, d\mathcal{H}^2(\boldsymbol{X}), \qquad \boldsymbol{x}(\boldsymbol{X}) = \boldsymbol{x}^0(\boldsymbol{X}) \quad \forall \boldsymbol{X} \in \partial_1 \Omega, \tag{11}$$

where W is a elastic free energy functional, $\mathbf{F} = \mathrm{grad}(\boldsymbol{\phi})$ the deformation gradient, $\mathbf{B}$ is the known or prescribed body force, $\mathbf{T}$ is the known or prescribed surface traction over the natural boundary ($\partial_1 \Omega$), $\boldsymbol{\phi}^0$ is a known or prescribed value of the deformation mapping along the essential boundary ($\partial_2 \Omega$), and $\lambda, \mathcal{H}^2$ are the Lebesgue (volume) and Hausdorff (area) measures, respectively.

We are presently interested in problems in which Ω is a non-trivial, time-varying, not necessarily simply connected, and not conserved. As discussed above, this can present numerical challenges, as discretization of Ω can become prohibitively complex. The diffuse interface method replaces the explicitly definition of Ω with an implicit definition via the support of $\eta_\epsilon : \mathbb{R}^3 \to [0, 1]$. The order parameter is characterized by a diffuse interface width parameter ϵ (here, the same as that used in the phase field regression model), and $\mathrm{supp}\, \eta = \Omega$ in the limit as $\epsilon \to 0$.

With these definitions in hand, the diffuse interface method results from the following replacements: first,

$$\Omega \mapsto \mathbb{R}^3 \qquad\qquad d\lambda(\boldsymbol{X}) \mapsto \eta \, dV \qquad\qquad d\mathcal{H}^2(\mathbf{X}) \mapsto -|\nabla \eta| \, dV. \tag{12}$$

where inherent diffusiveness of η has a smoothing effect on Ω and $\partial\Omega$, so it is no longer necessary to be as careful about the choice of measure used (hence the change to dV). Next, two other replacements are necessary:

$$\underbrace{\mathbf{B} : \Omega \to \mathbb{R}^3}_{\text{discrete}} \mapsto \underbrace{\mathbf{B} : \mathbb{R}^3 \to \mathbb{R}^3}_{\text{diffuse}} \qquad\qquad \underbrace{\mathbf{T} : \partial_2 \Omega \to \mathbb{R}^3}_{\text{discrete}} \mapsto \underbrace{\mathbf{T} : \mathbb{R}^3 \to \mathbb{R}^3}_{\text{diffuse}}, \tag{13}$$

that is, the domain of $\mathbf{B}, \mathbf{T}$ is no longer the interior of the body and the natural boundary, but all of $\mathbb{R}^3$. For $\mathbf{B}$ the replacement is trivial, as any finite value for $\mathbf{B}$ outside of Ω will vanish. The replacement is more complex for surface tractions. A simple yet robust choice is to set it equal to the extrusion of the original traction along the normal to the diffuse boundary,

$$\mathbf{T}(\boldsymbol{Y} \in \partial_2 \Omega) \mapsto \mathbf{T}(\boldsymbol{X} = \boldsymbol{Y} + s\boldsymbol{N}) \quad s \in [-\epsilon/2, \epsilon/2]. \tag{14}$$

This has the desired effect of causing $\mathbf{T}$ to vary along the boundary, but remaining constant along the normal to the boundary. So, with the diffuse boundary replacement, the diffuse potential energy becomes

$$\Pi[\boldsymbol{\phi}] = \int_{\mathbb{R}^3} \Big(\Big[\mathrm{W}(\mathbf{F}) - \boldsymbol{x} \cdot \mathbf{B} \Big] \eta + \boldsymbol{x} \cdot \mathbf{T} \, |\nabla \eta| \Big) \, dV. \tag{15}$$

The Euler-Lagrange equations follow by the application of the principle of minimum potential energy:

$$\mathrm{Div}\left(\eta \frac{\partial W}{\partial \mathbf{F}}\right) - \eta\,\mathbf{B} = \mathbf{T}\,|\nabla\eta| \quad \forall \boldsymbol{X} \in \mathbb{R}^3, \tag{16}$$

where $\mathbf{P} = \partial W/\partial \mathbf{F}$ is the Piola-Kirchhoff stress tensor, and Eq. (16) is the familiar stress-divergence equation for large deformations. It is possible (as shown in Agrawal and Runnels [25]) to impose essential boundary conditions ($\boldsymbol{\phi} = \boldsymbol{\phi}^0$) in a diffuse manner as well; however, as relevant cases are limited and complicate the formulation, we assume all essential boundaries (if any) are managed at the discrete domain boundary.

The justification for Eq. (16) is derived here from the intuitively apparent, but not rigorously justified, replacements Eqs. (12) and (13). An alternative precise derivation follows by application of Theorem 1 in Schmidt, Quinlan, and Runnels [26], which demonstrates (i) that the jump in traction induced by $\nabla\eta$ is balanced by a jump in the stress divergence that recovers the natural boundary condition, and (ii) that the normal governing equations are recovered in the support of $\eta = 1$, which approximates Ω. It may thus be shown that Eq. (16) reduces, in the sharp interface limit ($\epsilon \to 0$), to

$$\mathrm{Div}(\mathbf{P}) - \mathbf{B} = \mathbf{0} \quad \boldsymbol{X} \in \Omega \tag{17}$$

$$\mathbf{P}\,\mathbf{N} = \mathbf{T} \quad \boldsymbol{X} \in \partial_2\Omega \tag{18}$$

as long as the order parameter η satisfies certain properties, which are naturally satisfied by solutions to the phase field equations. For other applications, the reader is referred to [26]. This concludes the development of the governing equations for finite kinematics mechanics with diffuse boundaries.

The remainder of this section presents the constitutive model for thermomechanical response of SCPs. In the presence of the temperature gradients inherent to deflagration, it is necessary to account for thermal expansion. We adopt the kinematic decomposition

$$\mathbf{F} = \mathbf{F}^e\mathbf{F}^\alpha. \tag{19}$$

Both phases may be assumed to expand isotropically under temperature change, and so the thermal eigenstrain is approximated as $\mathbf{F}^\alpha = \alpha(T)\mathbf{I}$. Consequently, $\mathbf{F}^e = \alpha^{-1}\mathbf{F}$ is substituted for $\mathbf{F}$ in Eq. (16). As long as thermal expansion is isotropic, $\mathbf{F}^e$ and $\mathbf{F}^\alpha$ commute. If anisotropic expansion occurs, more careful study of the choice of multiplicative decomposition may be required.

The present application is concerned with the analysis of energetic composites at the mesoscale, in order to explicitly account for material heterogeneities. Diffuse boundaries are again used to account for different materials by

$$W(\mathbf{F}) \mapsto \sum_{n=1}^{N} \phi_n(\mathbf{X})\, W_n(\mathbf{F}), \quad \sum_{n=1}^{N} \phi_n = 1 \;\; \forall \boldsymbol{X}, \tag{20}$$

where the support of the smoothly-varying diffuse species fields ϕ_n corresponds to the domain occupied by material n, which is characterized by the elastic energy $W(\mathbf{F})$. In the present work, this infrastructure is used to regularize material boundaries to improve solvability, so that ϕ_n is one or zero everywhere except for the diffuse boundary between materials, characterized by width ζ. It was shown in [25, 28] that this works correctly for heterogeneous materials, and was applied to finite-strain materials in [29]. Here, $\phi_n = \phi$ and $\phi_n = 1 - \phi$, where ϕ is the same diffuse species field used for the phase field and thermal transport models.

To model the cured HTPB binder, a neo-Hookean hyperelastic model is used. The neo-Hookean model has the well-known elastic energy functional [30, 31]

$$\mathrm{W}(\mathbf{F}) = \frac{\mu}{2}\left(\frac{\mathrm{tr}(\mathbf{F}^T\mathbf{F})}{J^{2/3}} - \mathrm{dim}\right) + \frac{\kappa}{2}(J-1)^2, \tag{21}$$

where μ is the shear modulus, κ is the bulk modulus, F is the deformation gradient tensor, and $J = \det \mathbf{F}$. The variable $\mathrm{dim} = 2, 3$ differentiates between 2-dimensional and 3-dimensional computations, respectively. (Note that the choice of dim is arbitrary and is included mainly only for purposes of aesthetics.) Because HTPB is nearly incompressible, the bulk modulus κ tends towards infinity, which can cause numerical problems. These can be addressed by removing

Parameter name	Symbol	Combined	AP	HTPB
Thermal Conductivity $\left[\frac{\mathrm{J}}{\mathrm{m\,s\,K}}\right]$	k		0.4186 [32]	0.1463 [32]
Density $\left[\frac{\mathrm{kg}}{\mathrm{m}^3}\right]$	ρ		1957 [7]	920 [7]
Specific Heat $\left[\frac{\mathrm{J}}{\mathrm{kg\,K}}\right]$	c_p		1297.9 [32]	2418.29 [32]
Pre-exponential Factor [-]	A		1.45×10^5 [7]	1.04×10^3 [7]
Activation Energy [K]	E_A		11000 [6]	7500 [6]
Base Mass Flux $\left[\frac{\mathrm{kg}}{\mathrm{m}^2}\right]$	$\dot{m}_0$		1000	5000
$\hat{q}$ constant [-]	C_0	$C_0^\mathrm{D} = -0.3715 + \frac{\zeta_0}{\zeta}$	$C_0^\mathrm{AP} = 0.42$	C_0^HTPB =0.323
$\hat{q}$ pressure factor [MPa^{-1}]	C_1	$C_1^\mathrm{D} = 2.01$	C_1^AP =0.46	C_1^HTPB =1.114
$\hat{q}$ pressure square factor [MPa^{-2}]	C_2	C_2^D =-0.09906		
Ref. interface width [μm]	ζ_0	3.0	3.0	3.0
Shear Modulus [MPa]	μ		14191.376 [21]	2.465 [21]
Bulk Modulus [MPa]	κ		15162.134[21]	1368.519 [21]
Elastic Modulus [MPa]	E		32449.98[21]	7.4 [21]
Thermal Expansion Coef. [1/K]	α		2.217×10^{-5}[33]	5.1×10^{-6}[34]

Table 1
Thermal properties of AP and HTPB and combined diffuse interface region. Values with references indicate literature from which material properties were taken. Values without reference were measured or calibrated as part of this work.

the κ term entirely, and adding an incompressibility constraint $J = 1$, which is enforced using a Lagrange multiplier. However, in the context of solid propellant, damage mechanisms are activated long before incompressibility effects become apparent. Therefore, it is a reasonable approximation to simply choose a large yet finite value for κ. In the case of HTPB, κ is chosen to be several orders of magnitude greater than μ, and adjusted to preserve the Young's modulus.

The solution to Eq. (16) is found using Newton's method. As the system evolves (that is, as η, T change in time - note that neither viscous nor dynamic effects are considered here), this usually produces a gradual change in the stress state. This means that the solution for each solve can be used as the initial guess for each subsequent solve, which improves stability of the solver and reduces the number of required Newton iterations. On the other hand, topological transitions in the solution can produce abrupt changes in the deformation solution. In such cases, additional iterations or alternative solution strategies may prove necessary (though this has not been the case in the present work).

Naturally, once convergence is found for strain energy function, the stress and strain field can easily be obtained as For reporting purposes, the Green-Lagrange strain tensor and the Cauchy stress tensor, given by,

$$\mathbf{E} = \frac{1}{2}\left(\mathbf{F}^T\mathbf{F} - \mathbf{I}\right) \qquad \boldsymbol{\sigma} = \frac{1}{J}\mathbf{P}\mathbf{F}^T, \tag{22}$$

respectively, are used to report strain and stress in the Eulerian frame.

3. Computational methods

Advantages of diffuse boundary methods typically come at the expense of the requisite high resolution of the discretization scheme around the interface boundary. Convergence to tolerance of interface behavior usually requires ~8 cells across interface regions [26]. Without adopting a strategic discretization strategy, the computational cost is prohibitive.

Block-structured adaptive mesh refinement (BSAMR) provides an ideal computational framework for diffuse interface methods that is also eminently scalable. The results in this work are obtained using the Alamo multiphysics code, which has previously been developed by the authors [28, 35] and is based on the open-source AMReX framework [36]. For the time-varying portion of the code, the BSAMR framework provides temporal as well as spatial substepping, allowing for arbitrary refinement with no loss of stability. Mesh refinement is driven by the local gradients of the solution in time. As discussed in previous work [12], the criteria for the phase field order parameter and the temperature

fields are

$$\Big(|\nabla\eta||\Delta x| \geq 0.001 \quad \text{or} \quad |\nabla T||\Delta x| \geq 5.0\Big) \quad \text{and} \quad \eta > 0,$$

respectively, where Δx is the grid size. With the addition of the mechanics solver, an additional criterion is introduced:

$$\text{or} \quad |\nabla \mathbf{E}||\Delta x| \geq E_0 \quad \text{and} \quad \eta > 0,$$

where $|\nabla \mathbf{E}|$ is the Frobenius norm of the finite strain gradient and E_0 is a refinement parameter. In practice, it is better to avoid imposing Eq. (23), instead applying suitably conservative refinement conditions on η and T. This is because repeated **E**-driven refinement necessitates additional nonlinear mechanics solves, which are relatively expensive. It is typically well-worth the minor cost of additional refinement, especially since this adds the benefit of greater overall simulation fidelity.

Alamo utilizes explicit methods for time integration and finite difference methods for spatial discretization. Stability of the explicit, forward Euler time integration scheme is determined by the phase field method. It was previously determined to be

$$\frac{L\epsilon\kappa\Delta t}{\Delta x^2} < 1, \tag{24}$$

which is easily enforceable using the temporal substepping algorithm.

A unique aspect of this work is the use of a strong-form, finite difference geometric multigrid solver for implicit mechanics. This is distinct from the widely used finite element method, but offers numerous advantages. The linear kinematics formulation of this algorithm, using a "reflux-free" formulation of BSAMR, was presented in [28], and coupled to a Newton solver in [29]. The use of diffuse boundaries to solve near-singular problems for linear elasticity was recently demonstrated in Agrawal and Runnels [25]. Here, the near-singular algorithm in [25] is combined with the Newton solver in [29] for a complete general mechanics solver in a diffuse boundary, time varying context.

4. Results

This section presents the validation of the computational method by comparison to analytic and finite element results, followed by the application of the method to thermal and mechanical load during deflagration. The propellant results here are for AP/HTPB, but it should be noted that the method is not unique to this composition, and can be readily extended to other propellants of interest. Metal additives, such as aluminum, and other burn rate enhancers are not considered in this work, but the mechanics solver is sufficiently robust to handle such compositions as long as the interface regression and heat flux are also calculated correctly.

Validating the mechanical response during deflagration is a difficult task, as the difficulty of performing the requisite experiments for mesoscale *in situ* strains is prohibitive. On the other hand, a great deal more data is available for the bulk quiescent thermomechanical response of SCPs with known mesoscopic structure. Therefore, the validation of this work is based on the previous comparison to prior work of the regression model [12] and current validation of thermomechanical data against literature. Thus, the *in situ* mechanical response is left as a predictive result. (We note that all visualizations are generated using VisIt [37].)

4.1. Model verification: comparison to analytic solutions and finite element analysis

The finite kinematics elastic solver is validated by considering two test cases: that of a pressurized hole in an infinite plate (verified by comparison to theoretical solutions, testing the application of tractions on the diffuse boundary) and that of a plate with a hole subjected to clamped, uniaxial tension (verified by comparison to finite element analysis). In both, a two-dimensional neo-Hookean model with unitary constants ($\mu = 1$ and $\kappa = 1$) is used. To simplify the comparison, all values are nondimensionalized.

4.1.1. Pressurized hole in an infinite plate

To determine the hyperelastic response subject to a nonhomogeneous diffuse traction condition, the method is applied to the problem of a pressurized hole in an infinite plate. For this case, a hole with unitary radius is placed in an 8x8 plate. The order parameter is defined using a hyperbolic tangent function:

$$\eta = \frac{1}{2} + \frac{1}{2}\tanh\left(\frac{\sqrt{x^2+y^2} - R}{\varepsilon}\right) \tag{25}$$

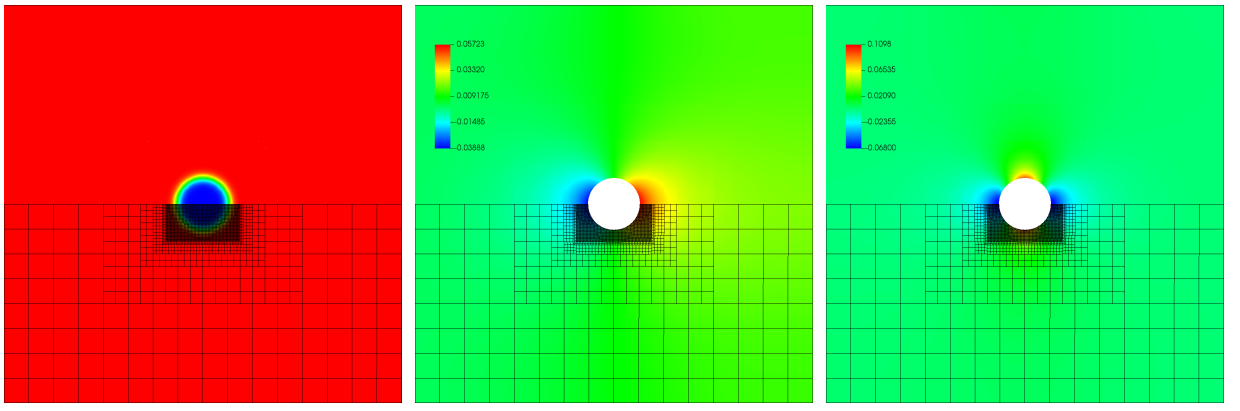

(a) Order parameter η (b) x-displacement field (c) xx-stress field

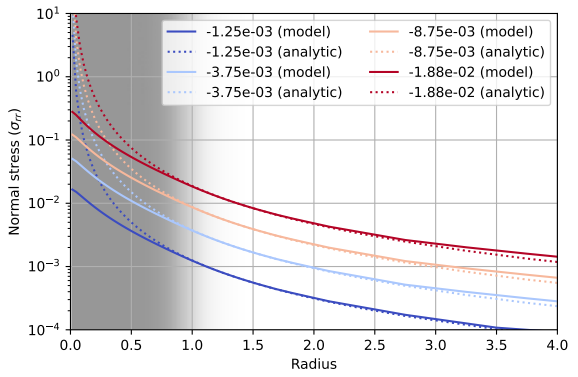

(d) Radial stress vs radius at different pressures

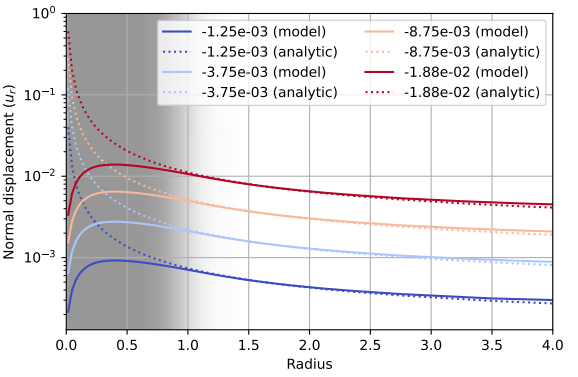

(e) Radial displacement vs radius at different pressures

Figure 1: Numerical solution for a pressurized hole compared to analytic Lamé solution for a linear elastic solid. The field variables are plotted in a-c along with the adaptively refined mesh. Radial values of stress and displacement are plotted in d-e and compared with the Lamé solution. The grayed out region indicates the hole, where $\eta = 0$, and in which neither the model nor the Lamé solution are valid.

with $R = 1.0$, $\varepsilon = 0.2$. Pressure is ramped from 0 to 0.1 at 0.00125 increments. This is sufficient to induce visible deformation. The base grid is 16x16 on the coarsest level, and five levels of BSAMR refinement are enabled to ensure adequate refine along the boundary (Fig. 1a). The response at maximum displacement is visualized in Cartesian coordinates: displacement in the x direction (Fig. 1b) and normal stress in the xx direction (Fig. 1c). The components in the y direction (rotated by 90 degrees) are identical.

To determine the accuracy of the solution quantitatively, the result is compared to the theoretical Lamé solution for an isotropic linear elastic material. The Lamé solution (as a function of radius r) is derived from the axisymmetric Airy stress function [38]

$$\Phi(r) = C_1\, r^2 + C_2 \ln(r) + C_3, \tag{26}$$

with constants C_1, C_2, C_3 determined by boundary conditions. This yields the following expressions for stresses and displacements:

$$\sigma_{rr} = 2C_1 + \frac{C_2}{r^2} \qquad \sigma_{\theta\theta} = 2C_1 - \frac{C_2}{r^2} \qquad u_r = \frac{1}{E'}\left[2(1-\nu')\,C_1\, r + (1+\nu')\frac{C_2}{r}\right]. \tag{27}$$

The material constants $E' = E/(1-\nu^2)$, $\nu' = \nu/(1-\nu)$ are the effective Young's modulus and Poisson's ratio, respectively, for a plate in plane strain. The infinite plate approximation implies that $C_1 \to 0$ (to prevent infinite displacement in the far-field). The remaining constant C_2 is solved by setting the traction boundary condition $\sigma_{rr}(1) = -C_2 = -p$.

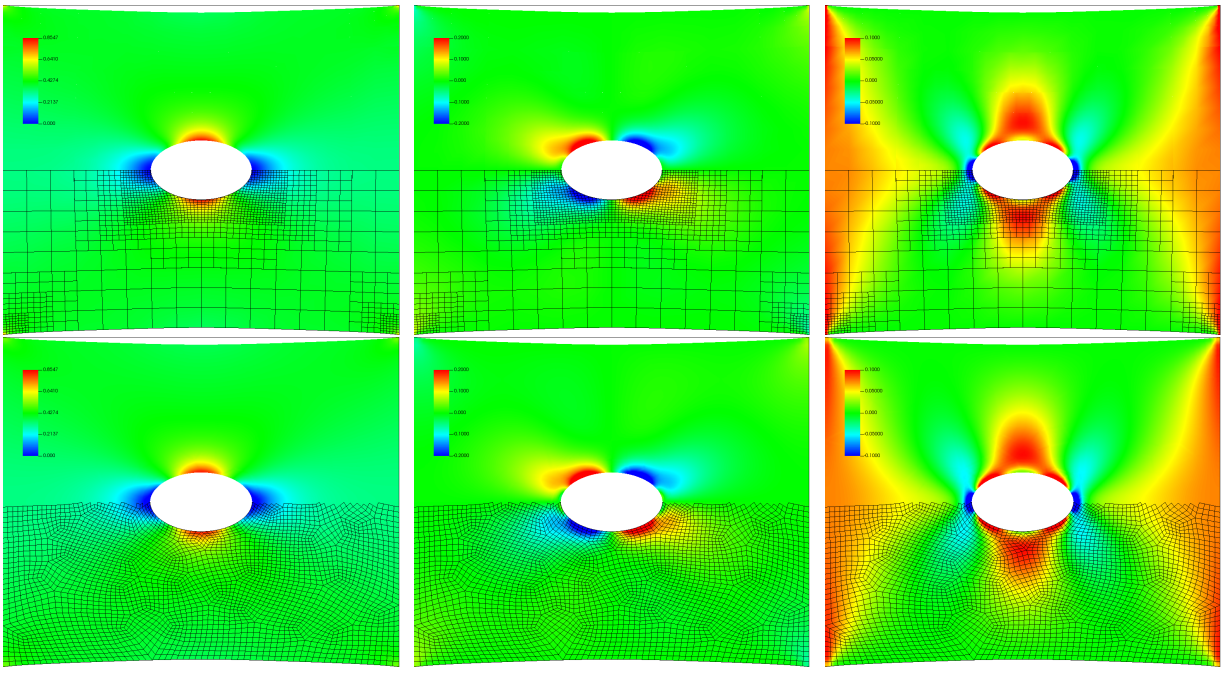

(a) σ_{xx} (b) σ_{xy} (c) σ_{yy}

Figure 2: Comparison of model results (top) to results from the finite element method (bottom) for a hyperelastic plate with a hole under uniaxial tension with clamped ends. Colors correspond to stress fields; displacement is visualized through deformation of the mesh.

The Lamé solution is compared to the numerical result for radial stress (Fig. 1d) and radial displacement (Fig. 1e). The order parameters is represented by the color of the background (gray corresponds to $\eta = 0$, white to $\eta = 1$); therefore, a good match is only expected within the white region. Nearly a perfect match in the stress is observed at the diffuse boundary. As the stress drops off, some divergence occurs. This is due primarily to the use of a logarithmic y scale, which exaggerates the error; however, it is also due to the finiteness of the computational domain. A similarly close match is observed in the displacement as well. Again, the departure is small, and most noticeable in the far-field.

4.1.2. Plate with hole under tension with clamped ends

Model verification against analytic solutions is limited for large deformation mechanics due to the lack of exact results for nonlinear elasticity. Therefore, results of the present diffuse boundary near-singular model are compared to the results of a traditional finite element solver. A unit square domain with a 0.01-radius hole in the middle is subjected to uniaxial tension imposed via fixed-grip boundary conditions on the edge of the domain. Displacements on the left side are all fixed; displacements on the right side are all fixed and set to up to 0.2 in the x direction (for a total of 20% strain). The same neo-Hookean model as above (with unitary moduli) are used in both the present model and the FEM model.

For the diffuse boundary model, a base grid of 16x16 is used with 3 additional BSAMR levels. Adaptive refinement is based on the gradient of η as well as the gradient of the strain; consequently, refinement occurred around the hole in the center as well as the four corners. For the finite element results, the standard finite element method using an an in-house finite element solver is used.[1] The mesh is generated using Gmsh [39]. The FEM mesh consists of second order two-dimensional quadrilateral elements with an interior node (Q9). No *a priori* refinement was used with the FEM mesh, but convergence was tested against meshes with lower resolution and lower order to ensure convergence.

Results were calculated for both methods; all three components of stresses are visualized on the mesh (using identical colormaps), which is deformed according to the calculated deformation field (Fig. 2). The results are nearly identical, with a couple of differences. First, the present model exhibits slightly higher stresses at the domain corners.

[1] The finite element code is available upon request.

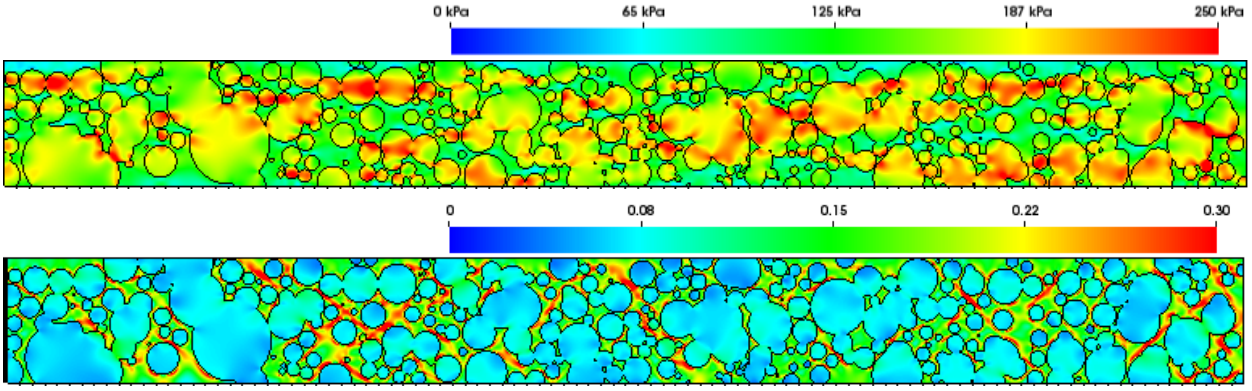

Figure 3: Uniaxial stress test. Von Mises stress (Top) and deviatoric strain (Bottom) at 20% strain.

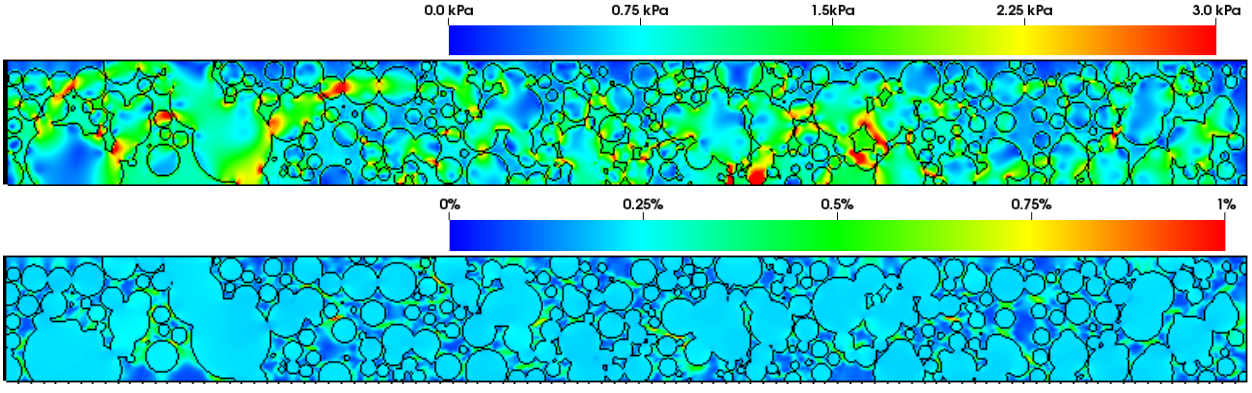

Figure 4: Thermal Expansion results for $\Delta T = 100K$. Von Mises stress (Top) and deviatoric strain (Bottom)

This is due to the fundamental difference between the strong form (used here) vs the weak form (used by FEM); whereas FEM shape functions tend to diffuse singularities, the present model does not. Second, there are some slight variances in the stresses very near to the diffuse boundary; however, these are present only in the support of $\nabla\eta$. Otherwise, the match is found to be nearly exact between models. Therefore, it is concluded that the model behaves as expected.

4.2. Model validation: uniaxial tension and thermal expansion tests

The model is validated against experimental data for uniaxial tension. Although literature documenting mechanical properties of AP/HTPB composites is surprisingly scarce, relatively recent data is reported in Kim and Im [40] that furnishes a suitable set of data for comparison against the mechanics model. To generate the computational domain in a manner that faithfully represents the experimental configuration, a 3D mesostructure is generated by randomly packing a rectangular domain (dimensions 10 mm x 1 mm x 1 mm) with spheres, 75% by volume. The distribution of the spheres follow the Miller packing (as described in [42, 43]). The domain is then sliced, producing the final 2D structures used here. These are then used as inputs to computationally determine the quasistatic response under uniaxial tension test, up to a maximum strain of 20%. Recall that meshing happens automatically as a result of the use of BSAMR, making it straightforward to generate arbitrarily complex mesostructures with virtually no processing time.

The mechanical response is calculated and displacement/strain/stress fields are resolved at each loading point (Fig. 3). It is apparent by inspection that the stress is concentrated along material interfaces normal to the x axis, and particularly, near to small quasi-laminate regions of HTPB binder. Though no mechanical failure model is considered in the present work, the stress results clearly indicate that strain localization at the binder/matrix interface is likely to precipitate the first failure response (which seems consistent with experimental findings [40, 44, 45]). While high-stress

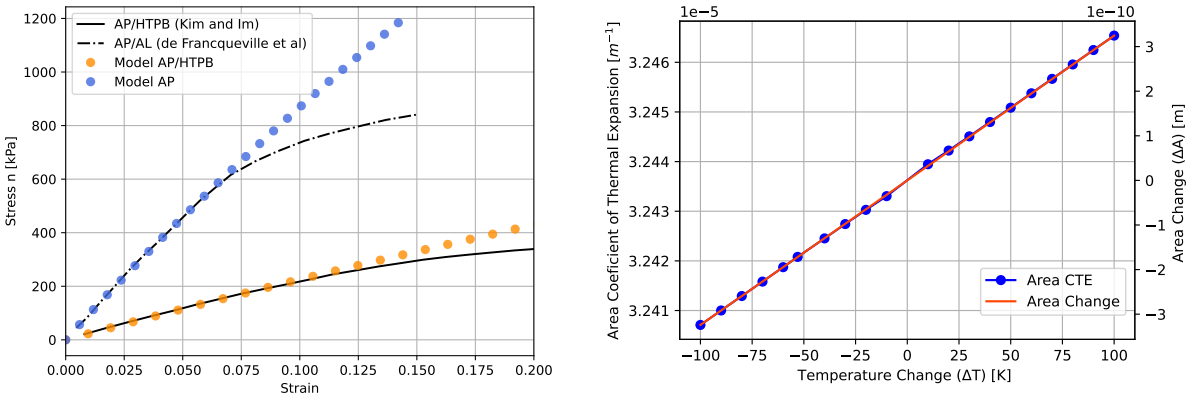

Figure 5: Comparison of Stress-Strain results with data from [40] and [41] (Left). Calculated thermal expansion coefficient and area variation as a temperature function (Right).

regions appear in both AP and HTPB, it is apparent that shear *strain* is highly localized within the HTPB binder. This appears to occur most frequently when HTPB is sandwiched between spheres of AP at a 45° angle to the normal, which is consistent with intuition and with classical mechanics theory.

The sample was also subjected to a thermal loading test to determine the aggregate coefficient of thermal expansion based on known values for AP and HTPB. A baseline initial temperature of 273K is set over the domain, and the temperature is then uniformly elevated in 10K intervals. This is repeated in the opposite direction, decreasing the temperature by 10K intervals, for a total of 100K in each direction. Mechanical boundary conditions are set so that the domain region is free to expand due to temperature change, and individual thermal expansion coefficients for pure AP and HTPB, as shown in Table 1, are used to define the system's initial eigenstrain. The resultant stress and strain fields illustrate the mechanical response due to CTE mismatch, and highlight potential failure sites (Fig. 4). The greatest stress appears to occur at regions of high curvature in the AP particles, generally when particles are overlapping or near to overlapping. The strain field shows primarily the difference in thermal expansion between AP and HTPB, where we see (as expected) that the AP expands to a greater degree. In only a couple of sites does any significant shear strain occur.

To quantify the accuracy of the model, the mechanical response of the model is compared to that in the literature [40] (Fig. 5). A quantitative comparison of the stress and strain values for the model against the experimental results in [40] can be performed (Fig. 5). There seems to be a close match in the mechanical response up to approximately 15% strain. As strain continues to increase beyond 15%, the computational and experimental results diverge, with the experimental mechanical response exhibiting a dropoff in stress. Typical loading under deflagration conditions is not expected to exceed 15% strain, and so the discrepancy is not particularly concerning. The most likely explanation for the difference is the presence of interfacial failure in the experimental composite (as discussed in [40] and [46]), which is not accounted for in the model. Though it is not the focus of (nor is it needed for) the present work, a closer match can certainly be attained through the use of damage models. We leave this as a recommendation for future work.

4.3. Thermomechanical response of packed spheres configuration during deflagration

In this section, the mechanics model is fully coupled to the phase field and thermal transport models to determine the elastic response in a SCP during regression. The same methods for mesostructure generation are used as in the previous section; the volume fraction in this packing is 65% vol. AP, and the domain dimensions are 1 mm x 1mm. Ignition is initiated through an imposed heat flux (laser) at the top boundary. The bottom, left, and right boundaries are treated as Neumann boundaries for the phase field equations and the thermal evolution model. For the mechanics model, all domain boundaries have sliding boundary conditions; that is, they prescribe zero displacement in the normal direction and zero traction in the tangential direction. After burn is initiated, the top domain boundary is irrelevant and is replaced by the diffuse boundary, which is traction-free.

The interface regresses with a thermal profile consistent with prior work [12] (Fig. 6a). As expected, heat flux is primarily concentrated at the species boundaries, causing spikes in temperature at the triple point between the burn surface and species interface. The burn interface continues to evolve throughout the domain in a similar fashion.

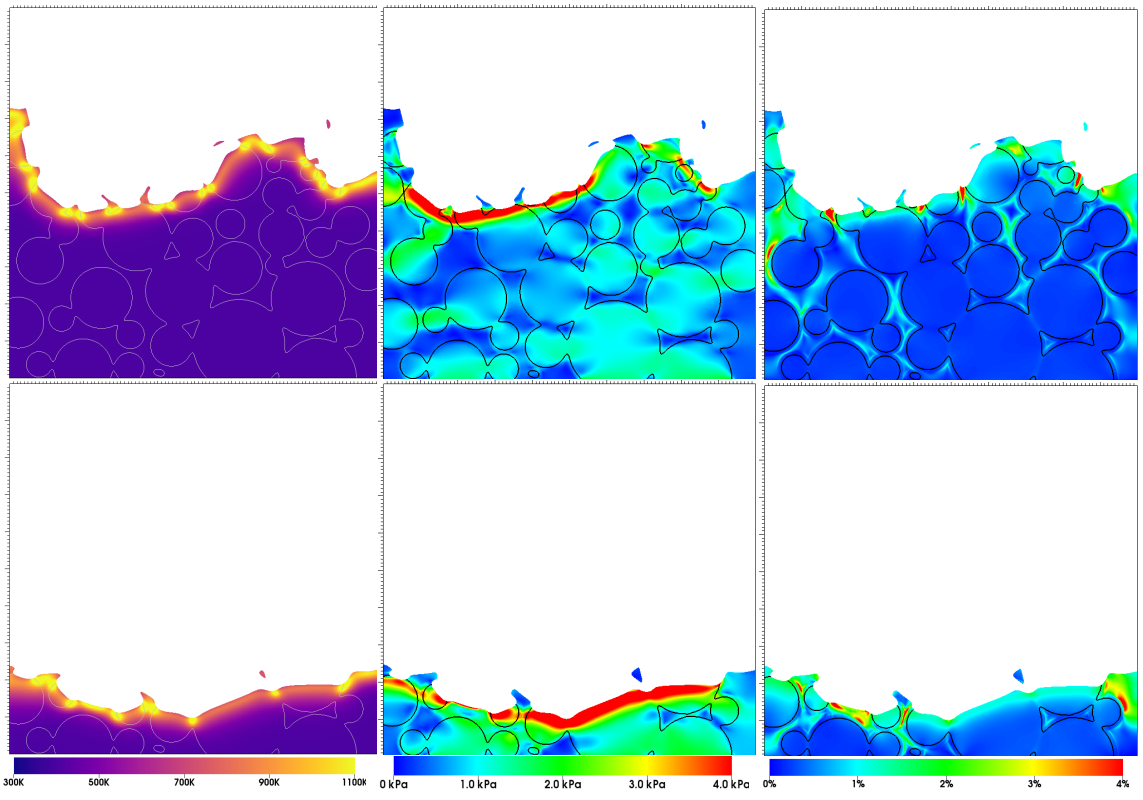

(a) Temperature (b) Von Misses Stress (c) Deviatoric Strain

Figure 6: Evolution of a 65 % AP mass fraction samples over the course of 0.2 seconds. Color corresponds to Temperature in a) and d), Von Misses stress in b) and e), and strain field in c) and f).

The mechanical response is driven entirely by the thermal loading, which causes the maximum von Mises stress to concentrate near the burn interface, as expected (Fig. 6b). The resultant stress profile at the burn interface does not exhibit any obvious correlation with mesostructure, and yet it nevertheless appears to be significantly influenced by it as evidenced by the localization of high stress regions. During the deflagration process, the maximum von Mises does not exceed 4 kPA, indicating that damage modeling is not necessary. However, it is conceivable that certain mesostructures could cause this threshold to be exceeded, and this would certainly be the case if combined with other mechanical loading. The deviatoric strain is also considered, as determined by the maximum deviatoric component of the Green-Lagrange strain tensor $\mathbf{E}$ (Fig. 6c). Predictably, the strain is highly localized in the HTPB binder, and the strain extends well ahead of the regressing interface. Most of the strain is on the order of 1-2%. The maximum strain is concentrated at the burn surface, reaching approximately 4%, again concentrated in the HTPB binder. While the strain is certainly large enough to warrant the use of nonlinear kinematics, on the other hand, it is well within the regime for which the mechanics model has been validated, as discussed in Section 4.2.

4.4. Thermomechanical response of a realistic mesostructure during deflagration

Much of the work done in SCP deflagration modeling has focused on idealized, packed spheres-type mesostructures that are statistically equivalent to those of real propellants. However, real-world propellants are usually quite far from idealized, and feature highly complex geometry. As shown in the previous section, the local particle geometry appears to have a quite significant influence on the local stress state during deflagration. Consequently, there is a need to consider realistic microstructures explicitly, in order to ensure that stress states are accurately assessed.

In this section, deflagration is simulated within a sample of propellant taken directly from the experimental literature. An scanning electron micrograph (SEM) image of an AP/HTPB/Al propellant, reported in [47], is considered (Fig. 7a). The dimensions of the domain are 1mm x 0.5mm. The present work does not consider Al, and so Al in the image is interpreted instead as AP, and so we expect that our predicted burning rate will be slower than that observed

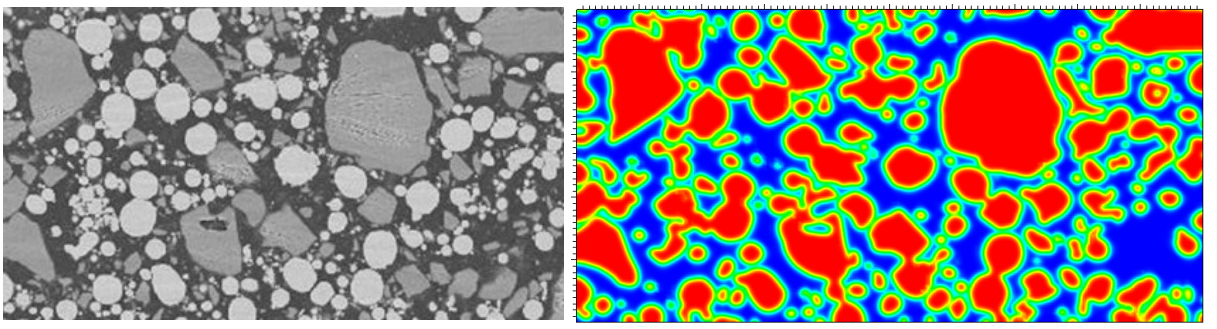

(a) (b)

Figure 7: Generation of model geometry for realistic propellant mesostructure a) SEM image for an aluminized AP/HTPB adapted from [47], and b) processed species field ϕ used in simulation. Used with permission.

experimentally. (More than two species can certainly be considered as far as mechanics modeling is concerned; the limitation is in the regression model.) The following steps are required: First, to convert the image to a suitable input for the model, the contrast is adjusted to binarize the image (i.e. make it black and white). Second, a Gaussian blur is then applied to the image to achieve the diffuse boundaries, where the degree of blur corresponds directly to the diffusiveness of the species field ζ (Fig. 7b). Third, the image is read directly by the code and used to generate the species field in the simulation. As with all results reported in this work, meshing happens automatically by BSAMR. Therefore, steps 1-3 can be performed entirely automatically, making it easy to examine a large variety of mesostructures.

This geometry is then used with the same regression model to determine the effects of realistic mesostructure on deflagration (Fig. 8). Overall, similar qualitative behavior is observed, especially in the thermal evolution, as in the packed spheres case. Note that this example considers a larger domain size, which is why the burn surface effects appear more localized. A prominent region of AP has the interesting effect of slowing the deflagration, as the heat flux in pure AP is less than that at the AP/HTPB interface, reducing the burn rate (Fig. 8b). The stress field (Fig. 8b) exhibits complex long-range behavior, influenced near the interface by the heat flux at the surface, but impacting the domain well inside the unburned region. The thermal stress along the interface is comparatively uniform, but there appear to exist certain regions within the propellant that transmit stress well advance of the burn front. This can also be seen by considering the strain field (Fig. 8c). Long fingers of strain localization - again, primarily in the HTPB binder - reach deep into the propellant, far ahead of the thermal wave at the interface. The maximum stress did not exceed 5kPa, and the maximum shear strain was at or below 3%, indicating again that the mechanical state was well within the validated regime for the mechanics model.

The volume of data generated by the model can prove cumbersome to process. One of the key desired outputs of the model is an overall assessment of the stress state in the propellant over its entire burn history. To achieve this, all of the stress states during deflagration are superimposed on top of each other and over the original input image (Fig. 9). A semitransparent color scale is used to represent the stresses, such that stress greater than 3.6 kPa is opaque, and below 3.6Kpa is rendered on a sliding transparency scale. The feathered appearance shows the intervals over which the elastic solves occur.

The complex nature of the evolving stress state appears to avoid any simplistic correlation to mesostructure; that is, one cannot immediately infer specific mesostructure characteristics that induce high stress regions. Stress is predominantly concentrated at or near regions of AP, as expected, and often near regions where there is a substantial amount of interface present. However, one can also identify seemingly identical regions that present substantially different mechanical response. We conclude that this is a result of the nonlinear impact of geometry on stress state, which underscores the importance of considering realistic geometries in regression modeling.

4.5. Effect of chamber pressure

The main focus of this work has been to isolate the effect of thermal expansion on the stress state. However, deflagration usually occurs in the context of high chamber pressure, which induces additional load on the interface. Hydrostatic pressure p manifests in the model (Eq. (16)) as a diffuse traction term, with

$$\mathbf{T} \mapsto -p\,\mathbf{N} \qquad\qquad \mathbf{T}|\nabla\eta| \mapsto -p\nabla\eta, \tag{28}$$

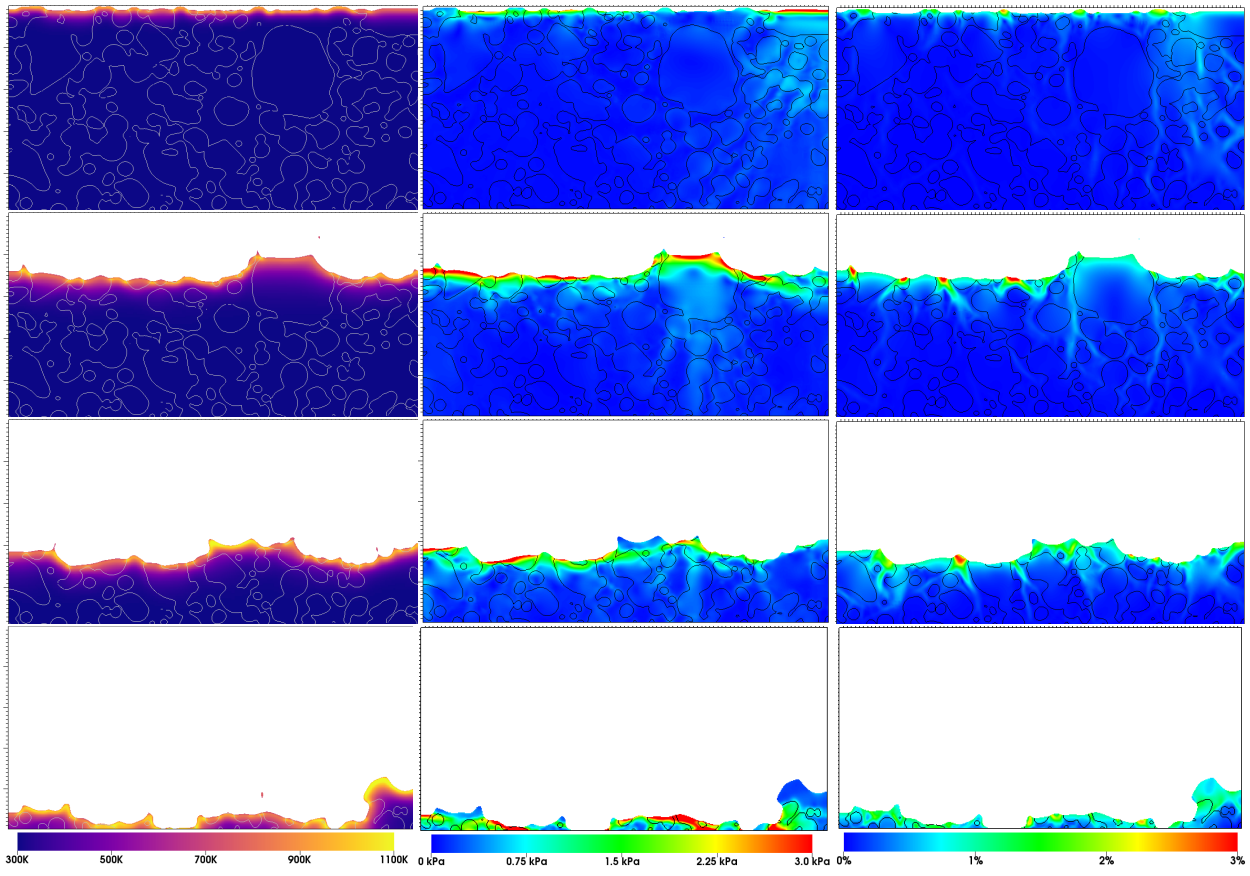

(a) Temperature (b) von Mises stress (c) Maximum shear strain

Figure 8: Elastic response for a regressing AP/HTPB with microstructure from SEM imaging. a) Von Misses stress field, and b) Deviatoric strain field

where $\boldsymbol{N} = \nabla\eta/|\nabla\eta|$ is the normal vector to the interface. (Note that terms arising from other mechanical effects, such as viscous drag from cross-flow, may be incorporated in a similar manner.) To test this, the realistic microstructure is then subjected to hydrostatic pressure ($p = 4MPa$) in addition to the thermal expansion (Fig. 10). The hydrostatic pressure increases the total Von Mises stress by a factor of 60-100%, and causes the high-stress regions to be distributed throughout the solid region. As expected, most of the deformation continues to be accommodated by the HTPB binder. This heterogeneity of the stress profile underscores the influence of propellant mesostructure.

5. Conclusion

In this work, a diffuse interface computational model for large mechanical deformation and for predicting the elastic response on regressing solid composite propellants is presented. The work uses the previously developed phase field model for regression, now combining it with a mechanics solver to determine the mechanical response during deflagration. The mechanics solver is based on the strong form equation for the conservation of momentum on a phase-field model and evaluated for a hyperelastic material using a Neo-Hookean model. The elastic solver is validated through comparisons to traditional FEM solvers for classical mechanical problems, and the combined model is then validated by comparison to experimental uniaxial tension test data before being applied to the problem of regression.

Two mesostructures are considered: an idealized structure consisting of packed spheres, and a realistic structure from the literature. Both exhibit qualitatively similar behavior, but it is apparent that the mechanical stress is highly influenced by the AP/HTPB geometry. Interestingly, the maximum stress appeared lower for the realistic propellant than for the idealized propellant (possibly because of the lack of sharp hypocyloidal regions that can result near overlapping

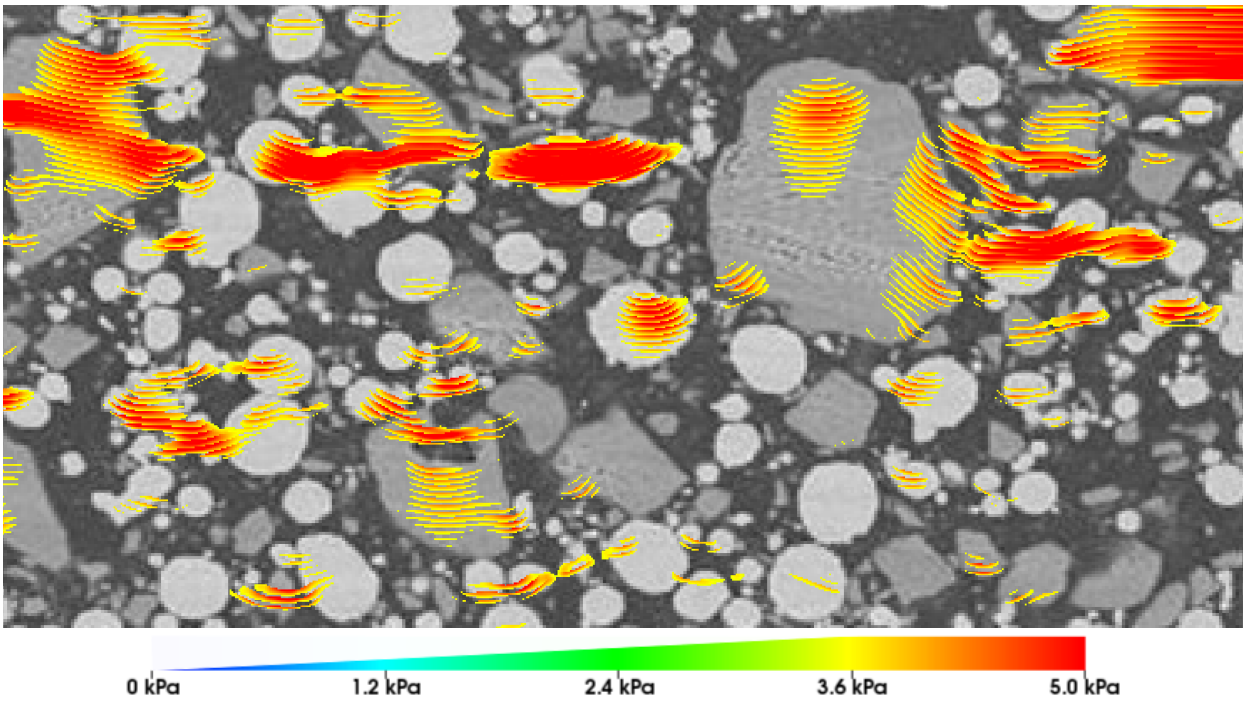

Figure 9: Superposition of von Mises stress concentration regions over time. At each time interval, stresses are visualized that exceed approx. 1.8 MPA, and this is repeated for all time intervals on the same image. Therefore, the stress contours do not represent a single stress state, but rather provide an estimation for localization of failure over the entire burn process.

spheres in the idealized case). Consideration of the stress evolution over time for the realistic propellant highlights the nonlinear effect of geometry, and the need for additional study of complex mesostructures.

We note the limitations in the present work. Because of this work's reliance on the phase field deflagration model, some of the same limitations are present as well: most notably, the use of a surrogate model for heat flux rather than fully resolving the gas phase. Another limitation is the lack of validation. While both the regression model and the mechanics model have been validated, the mechanical response during deflagration has not. There is, to the best of the authors' knowledge, no available data for comparison, nor does the technology even exist for measuring stress fields at the requisite resolution during deflagration. Until it validation is possible, then, these results are left as predictive.

6. Acknowledgments

The authors acknowledge support from the Office of Naval Research, grant # N00014-21-1-2113. This work used the INCLINE cluster at the University of Colorado Colorado Springs. INCLINE is supported by the National Science Foundation, grant #2017917.

References

[1] Alain Davenas, Development of modern solid propellants, Journal of propulsion and power 19.6 (2003), 1108–1128.

[2] Junyoung Hur, Jae-Beom Park, Gyoo-Dong Jung, and Sung-Kie Youn, Enhancements on a micromechanical constitutive model of solid propellant, International journal of solids and structures 87 (2016), 110–119.

[3] Ming Lei, Jianjun Wang, Jiming Cheng, Jinyou Xiao, Lihua Wen, Haibao Lu, and Xiao Hou, A constitutive model of the solid propellants considering the interface strength and dewetting, Composites Science and Technology 185 (2020), 107893.

[4] Shalini Chaturvedi and Pragnesh N Dave, Solid propellants: AP/HTPB composite propellants, Arabian Journal of Chemistry 12.8 (2019), 2061–2068.

[5] Birkan Tunç and Şebnem Özüpek, Implementation and validation of a three dimensional damaging finite strain viscoelastic model, International Journal of Solids and Structures 102 (2016), 275–285.

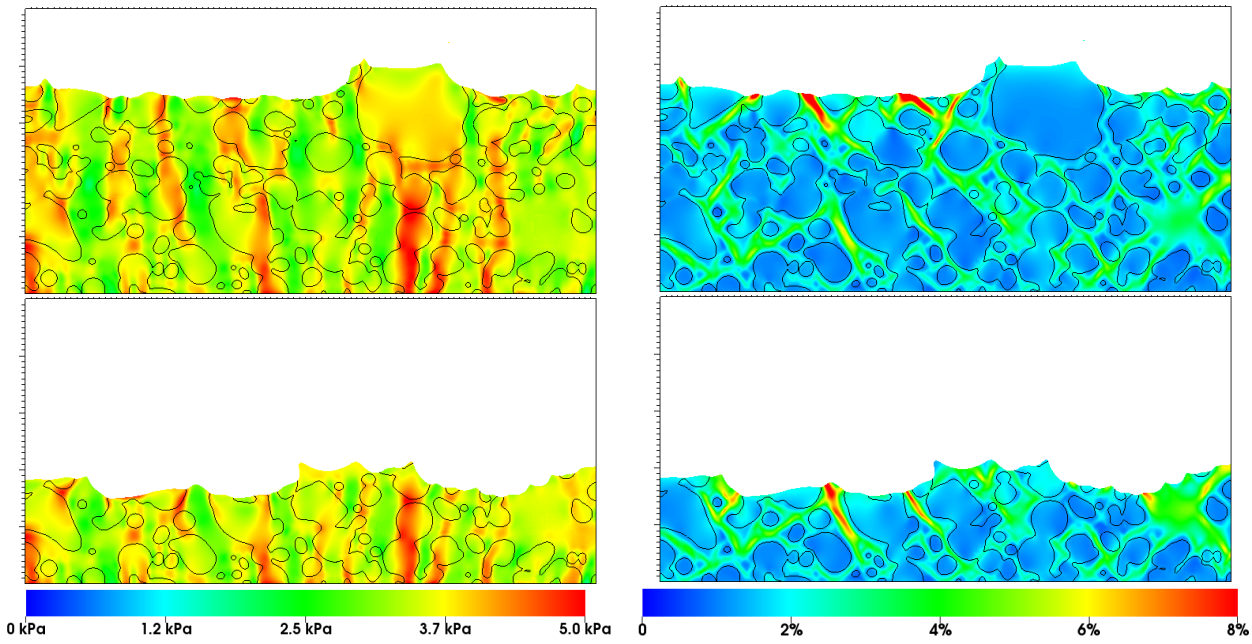

(a) von Mises stress

(b) Maximum shear strain

Figure 10: Simulation of elastic response due to thermal expansion and hydrostatic pressure for a regressing AP/HTPB composite with realistic mesostructure. a) Von Misses stress field, and b) Deviatoric strain field

[6] L Massa, TL Jackson, and M Short, Numerical solution of three-dimensional heterogeneous solid propellants, Combustion Theory and Modelling 7.3 (2003), 579.

[7] X Wang, TL Jackson, and L Massa, Numerical simulation of heterogeneous propellant combustion by a level set method, Combustion Theory and Modelling 8.2 (2004), 227.

[8] A Hegab, TL Jackson, J Buckmaster, and DS Stewart, Nonsteady burning of periodic sandwich propellants with complete coupling between the solid and gas phases, Combustion and Flame 125.1-2 (2001), 1055–1070.

[9] Tadbhagya Kumar, Chris H Rycroft, and Thomas L Jackson, Eulerian thermo-mechanical simulations of heterogeneous solid propellants using an approximate projection method, Combustion and Flame 219 (2020), 198–211.

[10] Chaitanya Vijay and PA Ramakrishna, Estimation of burning characteristics of AP/HTPB composite solid propellant using a sandwich model, Combust. Flame 217 (2020), 321–330.

[11] Baburaj Kanagarajan, J Matt Quinlan, and Brandon Runnels, A diffuse interface method for solid-phase modeling of regression behavior in solid composite propellants (2022).

[12] Maycon Meier, Emma Schmidt, Patrick Martinez, J. Matt Quinlan, and Brandon Runnels, Diffuse interface method for solid composite propellant ignition and regression, Combustion and Flame 259 (2024), 113120, ISSN: 0010-2180, DOI: https://doi.org/10.1016/j.combustflame.2023.113120, URL: https://www.sciencedirect.com/science/article/pii/S0010218023004959.

[13] KK Kuo, J Moreci, and J Mantzaras, Different modes of crack propagation in burning solid propellants, Journal of Propulsion and Power 3.1 (1987), 19–25.

[14] HL Berghout, SF Son, CB Skidmore, DJ Idar, and BW Asay, Combustion of damaged PBX 9501 explosive, Thermochimica Acta 384.1-2 (2002), 261–277.

[15] Mridul Kumar, Stephen M Kovacic, and Kenneth K Kuo, Flame propagation and combustion processes in solid propellant cracks, Aiaa Journal 19.5 (1981), 610–618.

[16] Juan Carlos Simo, On a fully three-dimensional finite-strain viscoelastic damage model: formulation and computational aspects, Computer methods in applied mechanics and engineering 60.2 (1987), 153–173.

[17] Sun Woo Park and Richard A Schapery, A viscoelastic constitutive model for particulate composites with growing damage, International Journal of Solids and Structures 34.8 (1997), 931–947.

[18] Shiang-Woei Chyuan, A study of loading history effect for thermoviscoelastic solid propellant grains, Computers & Structures 77.6 (2000), 735–745.

[19] Jinsheng Xu, Xiong Chen, Hongli Wang, Jian Zheng, and Changsheng Zhou, Thermo-damage-viscoelastic constitutive model of HTPB composite propellant, International Journal of Solids and Structures 51.18 (2014), 3209–3217.

[20] Gyoo-Dong Jung, Sung-Kie Youn, and Bong-Kyu Kim, A three-dimensional nonlinear viscoelastic constitutive model of solid propellant, International Journal of Solids and Structures 37.34 (2000), 4715–4732.

[21] K Matouš, HM Inglis, X Gu, D Rypl, TL Jackson, and Philippe H Geubelle, Multiscale modeling of solid propellants: From particle packing to failure, Composites science and technology 67.7-8 (2007), 1694–1708.
[22] Kyeong-Soo Yun, Jae-Beom Park, Gyoo-Dong Jung, and Sung-Kie Youn, Viscoelastic constitutive modeling of solid propellant with damage, International Journal of Solids and Structures 80 (2016), 118–127.
[23] KR Srinivasan, K Matouš, Philippe H Geubelle, and TL Jackson, Thermomechanical modeling of regressing heterogeneous solid propellants, Journal of Computational Physics 228.21 (2009), 7883–7901.
[24] Tadbhagya Kumar and Thomas L Jackson, Three-dimensional thermo-mechanical simulations of heterogeneous solid propellants, Combustion and Flame 233 (2021), 111590.
[25] Vinamra Agrawal and Brandon Runnels, Robust, strong form mechanics on an adaptive structured grid: efficiently solving variable-geometry near-singular problems with diffuse interfaces, Computational Mechanics (2023).
[26] Emma M Schmidt, J Matt Quinlan, and Brandon Runnels, Self-similar diffuse boundary method for phase boundary driven flow, Physics of Fluids (2022).
[27] Matthew L Gross and Merrill W Beckstead, Steady-state combustion mechanisms of ammonium perchlorate composite propellants, Journal of Propulsion and Power 27.5 (2011), 1064–1078.
[28] Brandon Runnels, Vinamra Agrawal, Weiqun Zhang, and Ann Almgren, Massively parallel finite difference elasticity using block-structured adaptive mesh refinement with a geometric multigrid solver, Journal of Computational Physics 427 (2021), 110065.
[29] Jared W Strutton, Newell H Moser, Edward J Garboczi, Abby R Jennings, Brandon Runnels, and Jena M McCollum, Interface History on Strain Field Evolution in Epoxy Resins, ACS Applied Polymer Materials (2022).
[30] Ronald S Rivlin, Large elastic deformations of isotropic materials IV. Further developments of the general theory, Philosophical transactions of the royal society of London. Series A, Mathematical and physical sciences 241.835 (1948), 379–397.
[31] Ronald S Rivlin and DW0042 Saunders, Large elastic deformations of isotropic materials VII. Experiments on the deformation of rubber, Philosophical Transactions of the Royal Society of London. Series A, Mathematical and Physical Sciences 243.865 (1951), 251–288.
[32] Luigi De Luca and Martin Summerfield, *Nonsteady burning and combustion stability of solid propellants*, vol. 143, AIAA, 1992.
[33] Robert Kellogg, Saul Lapidus, Trevor Hedman, and Joseph Kalman, Synchrotron based measurement of the temperature dependent thermal expansion coefficient of ammonium perchlorate, Propellants, Explosives, Pyrotechnics 45.3 (2020), 480–485.
[34] Katarzyna Gańczyk-Specjalska and Paulina Magnuszewska, An analysis of the mechanical properties of HTPB-propellants using DMA, Materiały Wysokoenergetyczne 12.2 (2020), 81–91.
[35] Brandon Runnels, *Alamo: Massively parallel implicit/explicit solid mechanics*, DOI: https://zenodo.org/doi/10.5281/zenodo.10381767,, URL: https://github.com/solidsgroup/alamo/,.
[36] Weiqun Zhang, Ann Almgren, Vince Beckner, John Bell, Johannes Blaschke, Cy Chan, Marcus Day, Brian Friesen, Kevin Gott, Daniel Graves, et al., AMReX: a framework for block-structured adaptive mesh refinement, Journal of Open Source Software 4.37 (2019), 1370–1370.
[37] Hank Childs, Eric Brugger, Brad Whitlock, Jeremy Meredith, Sean Ahern, David Pugmire, Kathleen Biagas, Mark Miller, Cyrus Harrison, Gunther H. Weber, Hari Krishnan, Thomas Fogal, Allen Sanderson, Christoph Garth, E. Wes Bethel, David Camp, Oliver Rübel, Marc Durant, Jean M. Favre, and Paul Navrátil, "VisIt: An End-User Tool For Visualizing and Analyzing Very Large Data", *High Performance Visualization–Enabling Extreme-Scale Scientific Insight*, 2012, pp. 357–372, DOI: 10.1201/b12985.
[38] Gabriel Lamé, Sur les surfaces isothermes dans les corps homogènes en équilibre de température, Journal de mathématiques pures et appliquées 1 (1897), 147–188.
[39] Christophe Geuzaine and Jean-François Remacle, Gmsh: A 3-D finite element mesh generator with built-in pre-and post-processing facilities, International journal for numerical methods in engineering 79.11 (2009), 1309–1331.
[40] Shin-Hoe Kim and Yong-Taek Im, Experimental study of material behavior of AP-HTPB base composite solid propellant, Journal of Mechanical Science and Technology 33 (2019), 3355–3361.
[41] Foucault de Francqueville, Julie Diani, Pierre Gilormini, and Aude Vandenbroucke, Use of a micromechanical approach to understand the mechanical behavior of solid propellants, Mechanics of Materials 153 (2021), 103656.
[42] Amanda L Dye, James E McClure, Cass T Miller, and William G Gray, Description of non-Darcy flows in porous medium systems, Physical Review E 87.3 (2013), 033012.
[43] SR Williams and AP Philipse, Random packings of spheres and spherocylinders simulated by mechanical contraction, Physical Review E 67.5 (2003), 051301.
[44] Zi-Jie Zou, Hong-Fu Qiang, Yi-Yi Li, and Xue-Ren Wang, Review on the Dewetting of the Particle-Matrix Interface in Composite Solid Propellants, Propellants, Explosives, Pyrotechnics 48.3 (2023), e202200270.
[45] EC Francis and CH Carlton, Some aspects of nonlinear mechanical behavior of a composite propellant. Journal of Spacecraft and Rockets 6.1 (1969), 65–69.
[46] Walid M Adel and Liang Guo-Zhu, Analysis of mechanical properties for AP/HTPB solid propellant under different loading conditions, International Journal of Aerospace and Mechanical Engineering 11.12 (2017), 1915–1919.
[47] Graham D Kosiba, Ryan R Wixom, and Matthew A Oehlschlaeger, High-Fidelity Microstructural Characterization and Performance Modeling of Aluminized Composite Propellant, Propellants, Explosives, Pyrotechnics 42.12 (2017), 1387–1395.